

1 CRYOEM STRUCTURE OF THE VIBRIO CHOLERAE TYPE IV
2 COMPETENCE PILUS SECRETIN PILQ

3 Sara J. Weaver^{1,5}, Matthew H. Sazinsky², Triana N. Dalia³, Ankur B. Dalia³, Grant
4 J. Jensen⁴.

5 ¹Division of Chemistry and Chemical Engineering, California Institute of
6 Technology, Pasadena, CA, USA, ²Department of Chemistry, Pomona College,
7 Pomona, CA, USA, ³Department of Biology, Indiana University, Bloomington, IN,
8 USA, ⁴Division of Biology and Biological Engineering and Howard Hughes
9 Medical Institute, California Institute of Technology, Pasadena, CA, USA, ⁵Present
10 address Howard Hughes Medical Institute, David Geffen School of Medicine,
11 Departments of Biological Chemistry and Physiology, University of California, Los
12 Angeles, CA, USA

13 **Abstract**

14 Natural transformation is the process by which bacteria take up genetic material
15 from their environment and integrate it into their genome by homologous
16 recombination. It represents one mode of horizontal gene transfer and contributes to
17 the spread of traits like antibiotic resistance. In *Vibrio cholerae*, the Type IV
18 competence pilus is thought to facilitate natural transformation by extending from
19 the cell surface, binding to exogenous DNA, and retracting to thread this DNA
20 through the outer membrane secretin, PilQ. A lack of structural information has
21 hindered our understanding of this process, however. Here, we solved the first ever
22 high-resolution structure of a Type IV competence pilus secretin. A functional
23 tagged allele of VcPilQ purified from native *V. cholerae* cells was used to
24 determine the cryoEM structure of the PilQ secretin in amphipol to ~ 2.7 Å. This
25 structure highlights for the first time key differences in the architecture of the Type
26 IV competence pilus secretin from the Type II and Type III Secretin System
27 secretins. Based on our cryoEM structure, we designed a series of mutants to
28 interrogate the mechanism of PilQ. These experiments provide insight into the

29 channel that DNA likely traverses to promote the spread of antibiotic resistance via
30 horizontal gene transfer by natural transformation. We prove that it is possible to
31 reduce pilus biogenesis and natural transformation by sealing the gate, suggesting
32 VcPilQ as a new drug target.

33 **Introduction**

34 Horizontal gene transfer, or the ability of microorganisms to directly share DNA
35 with one another, facilitates rapid evolution, can contribute to the development of
36 antibiotic resistance, promote the spread of virulence factors, and allow bacterial
37 pathogens to rapidly evade host immune response ¹. A clear understanding of the
38 mechanisms of horizontal gene transfer can aid the development of tools in the fight
39 against antibiotic resistance.

40 One mechanism of horizontal gene transfer is natural transformation, where a
41 competent bacterium can take up DNA from its environment and then maintain this
42 exogenous genetic material, either as a plasmid or by integrating it into the genome
43 by homologous recombination ². During transformation, DNA is actively brought
44 through the membrane. The requirements for DNA uptake vary with species, but
45 there is evidence for transformation of DNA from a few hundred base pairs up to
46 tens of thousands base pairs ²⁻⁵. Intergenous transformation can result in the
47 development of mosaic alleles that confer antibiotic resistance, and has been
48 demonstrated in a variety of genera, including *Streptococcus*, *Neisseria*, and
49 *Actinobacter*^{6,7}.

50 Additionally, natural transformation of large regions of DNA can induce serotype
51 switching in *Vibrio cholerae* ^{8,9} and in *Streptococcus pneumoniae* ¹⁰. The serotype
52 of a bacterial strain describes the immunodominant surface antigen that it displays,
53 and adaptive immune responses in human populations are generally serotype
54 specific. This has major public health implications, as serotype switching can help
55 bacteria evade the immune system. For example, after the introduction of a new
56 vaccine against a serotype of *S. pneumoniae*, epidemiologists traced a vaccine-

57 escape serotype to horizontal gene transfer ¹⁰. Thus, preventing horizontal gene
58 transfer represents a unique approach to mitigate the spread of antibiotic resistance
59 and virulence in bacterial pathogens.

60 Here, we focus our attention to the structural biology of natural transformation in
61 the gram-negative bacterium *Vibrio cholerae*. *V. cholerae* is the causative agent of
62 the diarrheal disease cholera ¹¹. Since 1817, cholera has spread globally in seven
63 pandemics that each feature strains of distinct characteristics. Natural
64 transformation in *V. cholerae* is tightly regulated and induced when these bacteria
65 are grown on chitin in their aquatic environment ¹². Chitin, a biopolymer found in
66 the exoskeletons of crustaceans, induces transcription of the chitin regulon and
67 expression of the Type IV competence pilus machinery ¹³. The Type IV
68 competence pilus machinery requires four elements: an inner membrane pilus
69 assembly complex, cytoplasmic motors to extend and retract the pilus, an outer
70 membrane pore (the secretin), and the pilus itself ¹⁴. The Type IV competence pilus
71 facilitates environmental DNA uptake by extending and retracting from the cell
72 surface through a large, outer membrane secretin pore called PilQ ¹⁵. To mediate
73 DNA uptake the pilus must translocate DNA across the membrane through the PilQ
74 secretin. Thus, the PilQ secretin represents a potential novel target to thwart this
75 mechanism of horizontal gene transfer.

76 The Type IV competence secretin is a member of the bacterial Secretin superfamily
77 ^{16,17}. Secretins are found in the Type II Secretion System (T2SS), the T3SS, the
78 Type IV pilus machine, and filamentous phage ¹⁸. Bacterial secretins are united by a
79 common C-terminal secretin domain that oligomerizes to form a large pore in the
80 outer membrane ¹⁹. The N-terminal protein domains form rings in the periplasm
81 and are thought to mediate interactions with other proteins ^{20,21}. While the C-
82 terminal secretin domain is remarkably similar across these secretion systems, the
83 N-terminal region varies (**Figure 1A**). The T2SS secretins have N-terminal protein
84 domains N0 to N3, followed by the secretin domain and then the S-domain. The
85 T3SS secretins lack the N2 domain, while the Type IV competence pilus secretins

86 lack the N1, N2, and S-domains. Additionally, the N-terminus of Type IV
87 competence secretins typically include one or more AMIN domains that interact
88 with the peptidoglycan²². These variations in domain architecture are likely related
89 to the specialization of different secretins²³. The T2SS exports periplasmic folded
90 proteins to the extracellular space. The T3SS uses a “needle and syringe” to export
91 cytosolic effector proteins outside of the cell, or directly into another cell. The Type
92 IV competence pilus extends and retracts a filament to take up DNA cargo.

93 The structure of the Type IV competence pilus secretin has been examined several
94 times, though no work has provided high-resolution details sufficient to model the
95 passage of DNA or to design inhibitors of this potential drug target. In 2012, a 26 Å
96 structure of *Neisseria meningitidis* PilQ was solved by cryoEM²⁰. In 2016, Koo *et*
97 *al.* solved the structure of *Pseudomonas aeruginosa* PilQ to 7.4 Å (pink in **Figure**
98 **2**). PaPilQ appeared to have 14 peripheral spokes lining the beta barrel that did not
99 demonstrate clear C14 symmetry, so C7 symmetry was assumed. In a 2017 paper,
100 D’Imprima *et al.* described the structure of *T. thermophilus* PilQ to ~7 Å resolution
101 with reported C13 symmetry (orange in **Figure 2**). D’Imprima *et al.* observed
102 flexibility between the N-terminal domains in TtPilQ that complicated the cryoEM
103 data analysis. Several high resolution cryoEM structures of bacterial T2SS and
104 T3SS secretins have been published, including *E. coli* GspD²⁴⁻²⁶, *V. cholerae*
105 GspD^{24,26}, *Pseudomonas aeruginosa* XcpQ²⁷, *Klebsiella pneumoniae* PulD²⁸, *A.*
106 *hydrophila* (pilotin-independent ExeD), *V. vulnificus* (pilotin-dependent EpsD)²⁹,
107 and *Salmonella typhimurium* (InvG)³⁰. Thus, to date, structural information about
108 the Type IV competence pilus secretin has mainly been inferred from the related,
109 but distinct T2SS and T3SS secretins.

110 Here, we present the structure of the *Vibrio cholerae* Type IV competence pilus
111 secretin PilQ to ~2.7 Å using a fully functional, His-tagged allele that we expressed
112 and purified from the native bacterium. Our work highlights differences between
113 the Type IV competence pilus, the T2SS, and the T3SS secretins, and emphasizes
114 the need for structures of different secretin family members. In particular we

115 discuss differences and remaining puzzles, including how the pilus could be
116 accommodated within PilQ during natural transformation and what part/s of the
117 secretin if any penetrate the outer membrane. Finally we report structure-inspired
118 designs of cysteine pair mutants that allowed us to reversibly inhibit pilus assembly
119 and natural transformation, presumably by sealing the secretin gate. These
120 experiments support the designation of VcPilQ as a druggable target, and more
121 broadly demonstrate how cysteine pair mutations can be employed to study the
122 activity of bacterial secretins.

123

124 **Results**

125 **Purification of *V. cholerae* PilQ in amphipol**

126 To ensure properly-folded and fully-function Type IV competence pilus machinery,
127 we chose to purify PilQ from *Vibrio cholerae* rather than a recombinant system. A
128 chromosomal mutation was made to add a deca-histidine tag to the N-terminus of
129 PilQ. The bacteria retained wild-type levels of natural transformation
130 (**Supplemental Figure 1A**). Previous work demonstrated that similar N-terminal
131 tags allowed for functional Type IV competence pilus activity¹⁵.

132 *V. cholerae* cells expressing PilQ were lysed in the presence of the surfactant n-
133 dodecyl β -D-maltoside (DDM). After affinity purification, PilQ was exchanged into
134 an amphipol environment. Secretins are detergent- and heat-resistant multimers
135^{31,32}. SDS page analysis of PilQ in amphipol showed a high molecular weight band
136 near the top of the gel (marked with an asterisk in **Supplemental Figures 1B, D,**
137 **and E**). Western blotting against the histidine tag on PilQ confirmed the high
138 molecular weight band as PilQ (marked with an asterisk in **Supplemental Figures**
139 **1C and F**). The gel electrophoresis also demonstrated some low molecular weight
140 species in the purified sample, some of which are detected on the Western blot and
141 presumed to be PilQ monomer or proteolyzed PilQ species that retained the N-
142 terminal histidine tag. Other bands on the SDS-PAGE not labeled in the Western,

143 likely represent PilQ fragments lacking the N-terminal histidine or contaminant
144 proteins. Regardless, the size difference between these contaminants (<100 kDa)
145 and the PilQ multimer (~860 kDa) made it easy to distinguish PilQ from the milieu
146 in electron micrographs (**Supplemental Figure 3A**).

147 To confirm that full length PilQ was present in our samples (residues 30-571 after
148 the 29 amino acid N-terminal signal peptide is cleaved), gel band analysis with a
149 trypsin digest and mass spectrometry was used to analyze the multimeric PilQ in
150 amphipol from a SDS page gel (band marked with an * in **Supplemental Figure**
151 **1D** was analyzed). The results demonstrated 65% sequence coverage, with
152 fragments identified in each domain of the folded protein from residues 50 to 567
153 (**Supplemental Figure 2**).

154 **Single particle cryoEM of the Type IV competence pilus secretin PilQ**

155 Here we report the high-resolution structure of the purified Type IV competence
156 pilus secretin VcPilQ by single particle cryoEM (**Figure 1**). The cryoEM data
157 processing steps are summarized as a flow chart in **Supplemental Figure 4** and in
158 Methods.

159 Briefly, *V. cholerae* PilQ (VcPilQ) was plunge-frozen on Quantifoil Holey Carbon
160 Grids with R2/2 spacing. A Titan Krios operating in a three by three pattern with
161 beam-image shift³³ was used to collect 3 movies per hole, resulting in 3,808
162 movies. The movies were motion corrected and screened for quality, which left
163 2,510 micrographs.

164 The cryoSPARC blob picker was used to identify 3,100,353 putative particle
165 location, several micrographs were inspected to adjust the threshold parameters to
166 select the top 252,319 particles for two-dimensional (2D) classification. 2D
167 classification demonstrated a wide variety of orientations, the clear presence of
168 secondary structure (**Supplemental Figure 3B**), and C14 symmetry
169 (**Supplemental Figure 3C**). After the initial 2D classification runs, 66,507 particles

170 were excluded from the dataset and used to generate a nonsense initial model
171 representing contamination. The 185,812 quality particles ('include') were used to
172 generate an initial model. A CryoSPARC heterogeneous refinement using the high
173 quality initial model and the contamination initial model was used to further clean
174 the dataset. Several rounds of 3D classification and 3D refinement were used to
175 select 100,543 particles for further analysis in Relion.

176 After polishing and CTF Refinement, the cryoEM structure (C14 symmetry, overall
177 resolution FSC@0.143 2.7 Å, FSC@0.5 3 Å, **Figure 2**) reached near-atomic
178 resolution and demonstrated isotropic resolution in the X, Y, and Z axes (3DFSC
179 sphericity 0.96) (**Supplemental Figure 5-6**)^{34,35}.

180 We were able to recognize and model residues 160 to 571 of PilQ (**Figure 1C**,
181 **Supplemental Movie 1**). Noting that residues 1-29 are cleaved (the N-terminal
182 signal peptide), our mass spectrometric analysis of the purified protein
183 (**Supplemental Figure 2**) demonstrated the presence of residues between 50 and
184 567, including the AMIN domain (residues 54-125) that is thought to interact with
185 the peptidoglycan in the periplasm²². While the AMIN domain was not resolved in
186 the PilQ structure, hazy density is present in the 2D classification in the region near
187 the PilQ N-terminus where we would expect the AMIN domain (marked with
188 asterisks in **Figure 1B**). Following the AMIN domain, residues 126-159 are
189 predicted by homology modeling to be unstructured (**Supplemental Figure 7**), so
190 they are also likely included in the hazy density. If that region is unstructured, it is a
191 likely source of the conformational heterogeneity observed as a hazy density in
192 **Figure 1B**. Extensive focused classification calculations were unable to improve
193 the resolution in this region (data not shown). Because the cell wall does not have a
194 crystalline structure, and the 14 AMIN domains around the ring must bind to it in
195 different places around the barrel, the AMIN domains are probably not regularly
196 arranged *in situ* either. In *Neisseria meningitidis*, the lipoprotein PilP is thought to
197 bind the AMIN domain and act as a bridge between the inner and outer membrane
198 components of the Type IV pilus machinery³⁶.

199 **The structure of VcPilQ demonstrates similarities to other secretins**

200 In each PilQ monomer, four beta strands come together to form a beta sheet
201 (**Figure 1C**). Once assembled, PilQ forms a 56-strand beta-barrel. Inside the barrel,
202 two further beta hairpins (beta strand-turn-beta strand each) form a gate. These
203 regions match the topology of other secretin structures (**Figure 3A-C**). Chimera
204 MatchMaker was used to align several published secretin structures to VcPilQ and
205 calculate the root-mean-square deviation (RMSD) between the C-alpha carbons of
206 each pair³⁷ (**Supplemental Figure 8**). In each case, the RMSD calculated over the
207 protein domains present in both structures (N3, secretin, and beta lip domains) was
208 about 1 Å. The outer membrane regions differ significantly, however, in both angle
209 and membrane spanning distance, as discussed in more detail below.

210 While their structures are similar, the electrostatic characteristics of the inner
211 surfaces of the T4P, T2SS and T3SS secretins vary (**Figure 3D**). The inner beta-lip,
212 N3, and coil regions of PilQ (**Figure 1C**) are all highly negatively charged (**Figure**
213 **3D**). In contrast, in the *V. cholerae* GspD and *E. coli* K12 GspD structures, there
214 are alternating negatively- and weakly positively-charged regions. These
215 differences are likely related to the function of PilQ in natural competence: the
216 DNA cargo of the Type IV competence pilus is also negatively charged, so it is
217 possible that this electrostatic repulsion will help the cargo pass through the cavity,
218 rather than getting stuck. By comparison, for T2SS secretins, the charge alternates
219 in the inner cavity.

220 **The N0 domain in VcPilQ agrees with previous structures**

221 The N0 domain of VcPilQ (residues 160 to 227) was resolved 4 to 7 Å local
222 resolution. This allowed us to build a model based on homology to previously
223 solved structures of N0 domains (**Figure 1C**), which includes a crystal structure of
224 isolated N0 domain from *Neisseria meningitidis* (4AR0)²⁰ (**Supplemental Figure**
225 **9**).

226 Only one of the seven T2SS secretins, and one of the T3SS published structures
227 resolves the N0 domain (Worrall et al. 2016, Chernyatina and Low 2019). Here we
228 can resolve the N0 domain (residues 160 to 227) of PilQ to 4 to 7 Å local
229 resolution, which allowed us to build a model based on homology to previously
230 solved structures of N0 domains (the cross-linked *Klebsiella oxytoca* PulD³⁸ and *S.*
231 *typhimurium* InvG³⁰), plus a crystal structure of an isolated N0 domain from
232 *Neisseria meningitidis* PilQ (4AR0)²⁰ (**Supplemental Figure 10**). Our VcPilQ N0
233 structure (**Figure 1C**) falls within 1.2 Å RMSD of each of the previous structures
234 (**Supplemental Figure 10E**).

235 **VcPilQ uses a novel helical coil to transition into the N3 domain**

236 In VcPilQ, a 32 Å alpha-helix follows the N0 domain (**Figure 1C**). None of the
237 T2SS or T3SS structures contain a helical coil to link N-terminal domains; instead
238 their periplasmic protein domains are linked by unstructured loops (**Figure 3**). This
239 difference was not anticipated, as homology models of VcPilQ based on other
240 structures more closely match the previously published T2SS and T3SS structures
241 (**Supplemental Figure 7**).

242 Following the end of this helix, the protein chain abruptly changes direction (~104°
243 angle) as the coil flows into the N3 domain (**Figure 1C**). This dramatically reduces
244 the channel diameter, from 90 Å at the bottom of the N0 domain to 60 Å across the
245 N3 domain (**Figure 4**). In the T2SS and T3SS structures, the diameter of the
246 channel is relatively constant.

247 **The putative outer membrane region of VcPilQ is thicker than T2SS secretins**

248 The secretin amphipathic helix lip (AHL) is thought to be a key determinant for
249 secretin outer membrane insertion and among Type IV pilus secretins, the AHL is
250 conserved¹⁸. The AHL is thought to mark the lower boundary of the outer
251 membrane region of secretins^{18,29,30}. The upper boundary of the outer membrane is

252 less clear since the micelle density in cryoEM reconstructions does not always
253 match the positions of aromatic residues²⁵.

254 In our VcPilQ atomic model, the distances between the bottom of the AHL to the
255 top of the beta strands is about 3 nm. As seen in **Figure 3C**, this putative outer
256 membrane region of VcPilQ is substantially taller than the same region in the
257 previously published T2SS structures. To investigate more than just the residue
258 locations, an inverted mask based on the atomic model density of VcPilQ was
259 generated and subtracted from the empirical cryoEM density, which reflects
260 unmodeled density in the cryoEM map that is not accounted for by the atomic
261 model (**Figure 4C**). This presumed micelle density (in grey) blooms around the
262 putative outer membrane region of the protein. This density appears both on the
263 outside of the beta barrel, and inside, coating the inner lip of PilQ. It remains
264 unclear which residues of PilQ are embedded within the outer membrane *in situ*
265 (see Discussion).

266 **Cysteine mutants indicate gate must open for pilus biogenesis and natural** 267 **transformation**

268 PilQ is thought to mediate DNA uptake during natural transformation in *V.*
269 *cholerae*. Blocking DNA uptake by inhibiting PilQ could prevent *V. cholerae* from
270 undergoing horizontal gene transfer in chitin biofilms, which can promote the
271 spread of antibiotic resistance genes and virulence factors. Toward this end, we
272 designed cysteine pair mutants to reversibly lock the gate with disulfide bonds. The
273 structure of VcPilQ was analyzed using the Disulfide by Design 2.0 web tool to
274 identify residue pairs with geometries that could support a disulfide bond³⁹⁻⁴¹. The
275 top hits from this screen were analyzed in Chimera and introduced into the *V.*
276 *cholerae* genome. Two cysteine pairs (S448C/S453C and L445C/T493C) were able
277 to assemble into PilQ multimers (**Figure 5**). The S448C/S453C pair is in the
278 proximal hairpin of the gate, likely crosslinking adjacent PilQ monomers(**Figure**
279 **5C, 5E**). The L445C/T493C pair likely crosslinks the upper and lower gate hairpins

280 of a single PilQ monomer(**Figure 5D, 5F**),. In both cases, under oxidizing
281 conditions, the cysteine pair mutants demonstrated lower transformation efficiency
282 than the control PilQ strain (**Figure 6A, Supplementary Figure 8**). Also, both
283 mutants exhibited reduced piliation (**Figure 6B**). High levels of the reducing agent
284 DTT were toxic to WT *V. cholerae* cells and inhibited piliation (**Figure 6B-D**) and
285 natural transformation (**Supplementary Figure 8**). However, when the cells were
286 grown with varying subinhibitory concentrations of DTT, the cysteine pair mutants
287 recovered transformation efficiency and piliation similar to the control parent strain
288 (**Figure 6C-D**). The S448C/S453C mutant is slightly more recalcitrant to DTT
289 rescue, which may be due to the fact that these cysteines are located further down in
290 the gate region making them less accessible to the reducing agent.

291 **Discussion**

292 Here we present the first high-resolution structure of a bacterial Type IV
293 competence pilus secretin. We observed key differences in the outer membrane
294 region and the periplasmic region among the different members of the secretin
295 family. These differences identify weaknesses in relying on homology models of
296 evolutionarily related secretins, like the T2SS secretin GspD, to understand PilQ.

297 **Homology modeling was insufficient to predict a Type IV Pilus Secretin** 298 **structure**

299 Before we solved the VcPilQ structure, we used homology modeling to predict the
300 structure of VcPilQ based on its sequence and the structures of previously solved
301 secretins⁴². The top five predictions are shown **Supplemental Figure 7**.
302 Comparing these predictions to our now-solved structure reveal significant
303 differences, including the thick outer membrane domain of VcPilQ and the extent
304 of the alpha helix between the N0 and N3 domains (**Supplemental Figure 7**).
305 Additionally, homology modeling cannot predict the three-dimensional
306 arrangements and orientations of the protein domains, the number of subunits, or
307 the inner barrel diameter. These features can be hypothesized based on T2SS or

308 T3SS secretin structures, but that strategy would neglect the clear variations in
309 selectivity and functionality across the Secretin superfamily. It is possible that
310 structural variability between secretins also indicates which regions of the protein
311 are more often repurposed by evolution to generate new function and/or selectivity.

312 **Outer membrane-spanning domain**

313 Curiously, in some previous secretin structures, the trans-outer-membrane region
314 appears to be only 2-3 nm thick (**Figure 3C**), which is much thinner than a typical
315 membrane. This has left it unclear which regions of secretin molecules are actually
316 embedded in the outer membrane, and whether any residues are exposed to the
317 extracellular surface. To investigate these questions, we used the Positioning of
318 Proteins in Membrane (PPM) web server to predict the location of the
319 transmembrane region of VcPilQ⁴³. The PPM web server result delineates the
320 hydrophobic region of the atomic model, which is shown by the dark horizontal
321 lines parallel to the membrane in **Figure 7**. The full lipid bilayer membrane will
322 then extend above and below these hydrophobic boundaries to account for the polar
323 head groups of the lipids. As we predicted based on the micelle density (**Figure**
324 **4B**), the lower boundary of the hydrophobic region is the amphipathic helix lip. The
325 upper hydrophobic boundary encompasses the beta strands of the beta lip, so the
326 loops likely protrude into the polar head groups.

327 Next we docked the VcPilQ structure into a sub-tomogram average of a closely
328 related PilQ imaged *in situ*. Recently, Chang et al. undertook an exhaustive
329 cryoelectron tomography (cryoET) study of the T4aP machinery in *Myxococcus*
330 *xanthus* (MxT4aP)⁴⁴. In the resulting sub-tomogram averages of the T4aP
331 machinery, the location of each component protein was identified. The domain
332 organization of MxPilQ is nearly identical to that of VcPilQ⁴⁵ (**Supplemental**
333 **Figure 11A**), but it has two more AMIN domains at its N-terminus (**Supplemental**
334 **Figure 11A**). The Phyre2 protein model of MxPilQ also looks remarkably similar

335 to the structure of VcPilQ solved here (**Supplemental Figure 11B**)⁴⁶, even though
336 the Phyre2 model was built independently.

337 We therefore docked the atomic model of VcPilQ into the sub-tomogram averages
338 of the non-piliated MxT4aP in *M. xanthus* $\Delta pilP$ (EMD-3249), the non-piliated
339 MxT4aP in *M. xanthus* $\Delta pilB$ (EMD-3260), and the pilated MxT4aP in wild-type
340 *M. xanthus* (EMD-3247) (**Figure 7A-C**)⁴⁴. Here we focus on the $\Delta pilP$ MxT4aP
341 sub-tomogram average (EMD-3249) because in this mutant only PilQ and TsaP
342 localize correctly, and are therefore the only proteins likely to be present in the sub-
343 tomogram average (**Figure 7A**)⁴⁴. The putative location of TsaP suggested in
344 Chang *et al.* 2016 is marked with an asterisk in **Figure 7**. In *M. xanthus*, TsaP is a
345 peptidoglycan-binding protein⁴⁷. In *V. cholerae*, the TsaP homolog LysM has not
346 been implicated in Type IV competence pilus function. The $\Delta pilB$ MxT4aP sub-
347 tomogram average (EMD-3260), which lacks the extension ATPase *pilB*, is also
348 shown because it was used to build a model of the non-piliated MxT4aP system
349 (PDB 3JC9) in Chang *et al.* 2016 (**Figure 7B**).

350 The atomic model of VcPilQ was docked into the MxT4aP sub-tomogram averages
351 using the predicted hydrophobic boundaries. At a high cryoEM density threshold,
352 the lipid bilayer is clearly observed as two leaflets in the MxT4aP sub-tomogram
353 averages (left in **Figure 7A-C**), so there is little doubt where the hydrophobic
354 region of VcPilQ should be placed in the sub-tomogram average. The bilayer
355 produces stronger features in the MxT4aP sub-tomogram averages than the protein,
356 so a lower cryoEM density threshold is required to visualize the full MxT4aP
357 machinery (right in **Figure 7**). In the non-piliated sub-tomogram averages (**Figure**
358 **7A-B**), VcPilQ agrees well with the MxPilQ density. The pilated MxT4aP clearly
359 undergoes a conformational change to accommodate the pilus in which the distance
360 between the inner and outer membranes increases (**Figure 7C**). In that case the
361 VcPilQ N0 domain doesn't extend far enough into the periplasm to line up with the
362 MxPilQ N0 domain (labeled in **Figure 7C**).

363 The gate region of VcPilQ nicely superimposes onto the gate of the *M. xanthus*
364 secretin, which suggests the VcPilQ structure was positioned correctly. However,
365 the putative outer membrane region in VcPilQ does not extend across the entire
366 outer membrane of the MxT4aP sub-tomogram averages. The thickness of the outer
367 membrane in the sub-tomogram averages ranges from 52 to 85 Å depending on the
368 cryoEM density threshold (labeled in **Figure 7A-C**), whereas the amphipol micelle
369 region in VcPilQ seems to be between 25 and 50 Å thick (**Figure 4B**). While this
370 discrepancy may be partially explained by the observation that the outer membrane
371 is about 5 nm thick in *M. xanthus* and 4 nm thick in *V. cholerae*⁴⁸, the shortness of
372 the other predicted trans-membrane domains of secretins (**Figure 3C**) and the two
373 bumps outside the outer membrane in the sub-tomogram average directly above the
374 secretin barrel (arrows in **Figure 7A** and **B**) call into question whether and how
375 parts of PilQ may penetrate the outer membrane *in situ*.

376 **VcPilQ could accommodate a Type IV Competence Pilus with gate** 377 **rearrangement**

378 The Type IV competence pilus machinery extends and retracts the Type IV
379 competence pilus through the PilQ outer membrane pore. In our structure of
380 VcPilQ in the absence of the pilus and accessory proteins, the inner diameter of the
381 channel ranges from 25 to 108 Å (**Figure 4A**).

382 The *V. cholerae* Type IV competence pilus is a Type IVa pilus. The major pilin
383 subunit in the T4aP is typically smaller than the major pilin subunits in the T4bP⁴⁹.
384 CryoEM structures of several Type IVa Pili (T4aP) have been solved from *N.*
385 *meningitidis* (NmT4aP, 6 Å resolution, 6 to 7 nm diameter), *N. gonorrhoeae*
386 (NgT4aP, 5 Å resolution, 6 nm diameter), *E. coli* (EHEC strain, EcT4aP, 8
387 Å resolution, 6 nm diameter), and *P. aeruginosa* (PaT4aP, 8 Å resolution, 5 nm
388 diameter)⁵⁰⁻⁵². Additionally, a recent preprint on bioRxiv studying Type IV pili in
389 *T. thermophilus* demonstrated the presence of narrow (4.5 nm) and wide (7 nm) pili
390⁵³. In **Figure 7D**, the EcT4aP cryoEM structure (yellow) is fit into our VcPilQ

391 structure (in grey)⁵². The gate region with diameters of 25 Å at the lower gate and
392 36 Å in the upper gate clashes with the pilus (**Figures 4A and 7D**). VcPilQ was
393 solved in the absence of the pilus, so this gate conformation likely represents a
394 “closed” state in cases where the pilus is absent or fully retracted. The next
395 narrowest region in the VcPilQ channel is across the periplasmic N3 ring (~60 Å in
396 **Figure 4A**). Some of the previously solved T4aP are 6 to 7 nm in diameter, which
397 would be a tight fit in this region. The N3 domain is connected to the secretin
398 domain by a loop, so it could possibly expand to accommodate a 70 Å pilus.

399 We used homology modeling to predict the VcT4aP monomer structure, but
400 because Neuhaus et al. reported both wide and narrow pili assembled by pilins
401 whose subunit structure are almost identical, we do not feel confident guessing the
402 VcT4aP diameter⁵³. Regardless, the gates in VcPilQ would have to move to
403 accommodate a pilus. Consistent with this notion, our disulfide locked cysteine pair
404 mutants could not extend pili in the absence of reducing agent, which strongly
405 suggests that the conformation adopted in the presented structure (in which these
406 cysteine pairs would be in close enough proximity to disulfide bond) represents the
407 closed gate conformation and cannot accommodate a pilus fiber. Additionally, the
408 sub-tomogram averaging of the MxT4aP demonstrates a secretin conformational
409 change with and without a pilus present (**Figure 7B-C**)⁴⁴.

410 In Yan *et al.*, a glycine in the VcGspD gate (G453) was identified as a putative
411 hinge point to facilitate gate opening, and showed that the G453A mutant trapped
412 the T2SS secretin in a partially open state²⁴. In our VcPilQ structure, the inner
413 channel distance between the corresponding glycine (G439) alpha carbons is about
414 8 nm (**Figure 4A**). Thus, we hypothesize that a gate hinge mechanism could
415 accommodate pili up to 7 nm in diameter. In an open state the gate loops could flip
416 up toward the extracellular space to accommodate the pilus.

417 **Conclusion**

418 Here we report the first high-resolution structure of a Type IV competence pilus
419 secretin, *V. cholerae* PilQ. This protein complex facilitates DNA uptake into
420 diverse bacterial species to aid in their evolution, and thus, represents a potential
421 target for therapeutic intervention. The *V. cholerae* Type IV competence pilus is a
422 model system to study natural transformation in bacteria. We identify key
423 differences between VcPilQ and the previously published structures of T2SS and
424 T3SS secretins. We designed cysteine pair mutants to reversibly seal the VcPilQ
425 gate and inhibit natural transformation, which can be used as a tool to further
426 investigate the function of the Type IV competence pilus machinery *in situ*. We
427 suggest a structural rearrangement that would transition our closed VcPilQ into a
428 piliated state that could accommodate previously solved structures of Type IV pili.
429 We also compare our structure to previous T4aP sub-tomogram averaging results in
430 *M. xanthus* which call in question which parts if any of PilQ extend across the outer
431 membrane. Together, these results elucidate the structure of PilQ and provide
432 mechanistic insight into natural competence in *V. cholerae*.

433

434 **Figure Captions**

435 **Figure 1: CryoEM structure of the *V. cholerae* Type IV Competence Pilus** 436 **Secretin PilQ**

437 **(A)** Protein domain organization in the Type IV competence pilus machine, the
438 Type II Secretion System (T2SS) and the Type III Secretion System (T3SS). The
439 AMIN domain (red), the N0 (or STN) domain (blue), the Secretin_N domains N1
440 (purple), N2 (brown), and N3 (green), the secretin domain (yellow) and the S
441 domain (pink) are shown.

442 **(B)** Example 2D classes show PilQ from the side (left) and from the top (right). The
443 outer membrane is indicated with OM. Asterisks indicate the putative AMIN
444 domains.

445 **(C)** The atomic model of the *V. cholerae* PilQ multimer is shown (right). One chain
446 is shown by itself (left). The outer membrane is represented in a light blue
447 rectangle. Dashed lines represent the different domains of the PilQ structure: AMIN
448 (not shown), N0 (grey/dark blue), coil (purple), N3 (green), Secretin (yellow), Beta-
449 lip (sky blue). The gate is labeled on the monomer.

450 **(D)** Model and cryoEM density of symmetrized PilQ is shown from the side (left)
451 and cut through the center (right).

452 **Figure 2: Comparison of VcPilQ to *P. aeruginosa* and *T. thermophilus* PilQ** 453 **structures**

454 Comparison of cryoEM density of PilQ structures from *V. cholerae* (left,
455 grey)(this study), *Pseudomonas aeruginosa* (magenta, center) (Koo et al. 2016),
456 and *Thermus thermophilus* (orange, right) (D'Imprima et al. 2017). In **(A)**, the
457 inside cavity of the cryoEM densities are shown, while **(B)** highlights the gate
458 region with a cut through the center of the density. The membrane is blue.

459 **Figure 3: Comparison of VcPilQ to T2SS and T3SS secretins**

460 The structures of VcPilQ (this study, dark red), *V. cholerae* GspD (5WQ8)
461 (green), *E. coli* K12 GspD (5WQ7) (blue), and *S. typhimurium* InvG (6DV3)
462 (yellow) (Jurrus et al. 2018; Worrall et al. 2016; Yan et al. 2017) are compared.
463 The putative outer membrane location is depicted as a blue rectangle. The
464 structures are shown as multimers **(A)** or monomers **(B)**. In **(C)**, the multimer is
465 shown in tan with one subunit colored. The outer membrane region is highlighted to
466 show that VcPilQ (left, red) has a ~ 30 Å membrane spanning distance, while
467 VcGspD, EcGspD, and StInvG have about a 24 Å membrane spanning distance.

468 **(D)** Adaptive Poisson-Boltzmann Solver was used to calculate the electrostatic
469 potential calculation of each secretin (Jurrus et al. 2018). The inner cavity of each
470 secretin is shown. The scale varies from -5 (red) to +5 (blue) in units of K_bT/e_c .

471 **Figure 4: Dimensions of the VcPilQ inner channel and outer membrane region**

472 **(A)** A central slice of the atomic model of *V. cholerae* PilQ colored as in **Figure 1**.
473 The inner cavity distances are depicted with dashed lines and labeled in Ångstroms.
474 The outer membrane is depicted as a blue rectangle.

475 **(B)** VcPilQ micelle density with putative outer membrane diameter labeled in Å.
476 The non-protein cryoEM density of VcPilQ is shown in grey at four different
477 Chimera thresholds (left to right). The atomic model of VcPilQ is shown in blue
478 and yellow according to the color scheme of **Figure 1**. In each image, yellow
479 spheres mark the approximate top and bottom of the micelle density. The distance
480 between the yellow spheres (dashed line) is shown below each image in Ångstroms.

481 **Figure 5: Design of cysteine pair mutants to lock the gate**

482 The atomic model of VcPilQ is shown as one chain **(A)** or as a multimer **(B)**. In **(C)**
483 and **(E)**, the S448C/S453C mutant, which locks the lower gate, is shown. In **(D)** and
484 **(F)**, the L445C/T493C mutant, which links the upper and lower gates, is shown. In

485 (A), the upper and lower gate are highlighted in a dashed line box. A zoomed in
486 region of this box is shown in (C) and (D) with the cysteine pair mutant residues
487 highlighted in red. In (B), the dashed line rectangle highlights the gate region,
488 which is shown on the left after a 90° rotation about the x axis. The coordinate
489 system is shown. This gate region is shown in (E) and (F) with the cysteine pair
490 mutant residues highlighted in red.

491 **Figure 6: Cysteine pair mutants lock the gate, reduce piliation, and reversibly**
492 **inhibit transformation**

493 (A) The transformation frequency of two cysteine pair VcPilQ mutants
494 (S448C/S453C on the left and L445C/T493C on the right) is plotted. Data are
495 normalized to the parental strain that expresses wild-type VcPilQ. Natural
496 transformation assays were performed in the presence of varying concentrations of
497 DTT (0 to 1.0 mM). Data are from at least 4 independent biological replicates and
498 shown as the mean \pm SD. The dashed line indicates the transformation frequency
499 expected if mutants are equivalent to the parental strain expressing wild-type
500 VcPilQ. Statistical comparisons were made by one way ANOVA with Tukey's post
501 test. * = $p < 0.05$, *** = $p < 0.001$. (B)-(D) Representative phase contrast (top) and
502 epifluorescence images (bottom) of *V. cholerae* pilA-Cys cells containing the
503 indicated mutations in PilQ when grown in the presence of (B) 0mM, (C) 1mM, or
504 (D) 2mM DTT prior to labeling with AF488-maleimide to visualize bacterial pili.

505 **Figure 7: Comparison of VcPilQ with sub-tomogram averages of *M. xanthus***
506 **Type IVa pilus machinery, and with the *E. coli* Type IVa pilus**

507 Sub-tomogram averages of the Type IVa pilus machinery in various *Myxococcus*
508 *xanthus* strains are compared with VcPilQ⁴⁴. VcPilQ is compared with the non-
509 piliated strains $\Delta pilP$ (A, EMD-3249) and $\Delta pilB$ (B, EMD-3260), and with the
510 piliated wild-type strain (C, EMD-3247). In the $\Delta pilP$ strain, only PilQ and TsapP
511 are present in the complex. The putative TsapP location is marked with an asterisk in
512 the rightmost volume in (A), (B) and (C). The location of the PilQ N0 domain is

513 marked with arrowheads. In **(B)** and **(C)** the location of the MxPilN and MxPilO
514 proteins are marked with arrowheads. Each Mx sub-tomogram average structure is
515 depicted at a high cryoEM threshold (left) to delineate the inner and outer leaflets of
516 the outer membrane, and at a lower cryoEM threshold (right) to fully reveal the
517 protein features. For each cryoEM threshold, a dashed line is used to indicate the
518 apparent membrane thickness, which ranges from 52 Å to 85 Å. The structure of
519 the VcPilQ solved here is shown with coloring like in **Figure 1**. **(D)** A central slice
520 of the cryoEM density of VcPilQ (grey) is shown with the *E. coli* Type IVa pilus
521 structure (yellow) fit in⁵². The outer membrane is depicted as a blue rectangle.

522 **Supplemental Figure 1: Expression and purification of VcPilQ from *V.***
523 ***cholerae* cells**

524 **(A)** The functionality of N-terminally deca-histidine tagged native PilQ was
525 assessed via natural transformation assays. These data indicate that the tagged
526 variant supports equal rates of transformation compared to an isogenic parent
527 strain, thus indicating that it is fully functional. Data are from four independent
528 biological replicates and shown as the mean ± SD. Statistical comparisons were
529 made by unpaired Student's t-test. NS = not significant. **(B-F)** Gel electrophoresis
530 analysis of VcPilQ in amphipols by coomassie stain **(B)**, **(D)**, **(E)**, and western
531 blotting against anti-His tag **(C)**, **(F)**. The multimer band is indicated with an
532 asterisk.

533 **Supplemental Figure 2: *V. cholerae* PilQ sequence with mass spectroscopy**
534 **results.**

535 Mass spectrometry coverage of purified PilQ: The sequence of VcPilQ (571 amino
536 acids) is shown in black with residue numbers marked ever 10 residues. Regions of
537 the sequence corresponding to protein motifs (Signal Peptide, AMIN Domain,
538 STN, Coil, Secretin_N and Secretin) or folded regions of the protein structure (N0,
539 N3) are highlighted with flags below the relevant sequence. The sequence coverage
540 achieved by mass spectrometry is highlighted with grey flags labeled "MS".

541 Approximately 65% of the sequence was represented in the peptides analyzed by
542 mass spectrometry. The protein sequence was visualized using the Benchling
543 Biology Software.

544 **Supplemental Figure 3: CryoEM data**

545 **(A)** Representative micrograph with a 10 Å low pass filter applied. A representative
546 Fourier transform and contrast transfer function (CTF) fit of the micrograph is
547 shown in the upper left corner. Scale bar, 200 Å. **(B)** Representative 2D classes
548 calculated in Relion. The 2D class box is 441.6 Å wide. **(C)** A top view 2D class
549 from demonstrates that VcPilQ has C14 symmetry. Yellow lines point to inner
550 spokes in the PilQ gate. Each monomer is numbered in white.

551 **Supplemental Figure 4: CryoEM data processing flow chart**

552 The major steps in data processing are summarized in a flow chart.

553 **Supplemental Figure 5: Fourier Shell Correlation and 3DFSC of VcPilQ**

554 **(A)** Fourier shell correlation (FSC) of VcPilQ cryoEM structure. **(B) to (D)** The
555 Salk institute 3DFSC server was used to examine the resolution in the X, Y and Z
556 dimensions in the VcPilQ structure(Tan et al. 2017). The sphericity is 0.962 out of
557 1.

558 **Supplemental Figure 6: Local resolution of VcPilQ**

559 ResMap was used to calculate the local resolution per voxel of the density map.
560 Resolution is plotted from 2.4 Å (cyan) to 8.4 Å (black). VcPilQ is shown from
561 the side **(A)**, as a central slice **(B)**, from the top (extracellular side, **C**) and from
562 the bottom (periplasmic side, **D**).

563

564

565 **Supplemental Figure 7: Homology modeling of VcPilQ**

566 I-TASSER was used to predict the structure of *V. cholerae* PilQ. I-TASSER
567 reported five potential models (labeled VcPilQ Homology model 1 to 5 and shown
568 with gray background). The ITASSER models are based on structures deposited in
569 the PDB, so the five models can be sorted by their similarity to the T2SS with the
570 cap (*Vibrio*-type), without the cap (*Klebsiella*-type) or the T3SS, so the models are
571 shown next to the corresponding secretin type. On the right the structure of VcPilQ
572 solved in this paper is shown in dark red. The membrane is blue.

573 **Supplemental Figure 8: Raw transformation frequency data for cysteine pair**
574 **mutants.**

575 Transformation assays were performed with the indicated strains in the presence of
576 DTT as indicated above the bars. Data are from at least 4 independent biological
577 replicates and shown as the mean \pm SD.

578 **Supplemental Figure 9: RMSD of VcPilQ versus published secretin structures.**

579 The monomer structure of VcPilQ (dark red) was aligned to the *E. coli* K12 GspD
580 (5WQ7) (A), the *V. cholerae* GspD (5WQ8) (B), and the *S. typhimurium* InvG
581 (6DV3 and 5TCQ) (C-D) (Worrall et al. 2016; Yan et al. 2017; J. Hu et al. 2018).
582 Only the N3 and Secretin domains were compared. RMSD was calculated with
583 MatchMaker in Chimera. The RMSD results are summarized in Table (E).

584 **Supplemental Figure 10: Alignment of VcPilQ N0 domain compared to**
585 **others.**

586 The VcPilQ coil and N0 domain (red, residues 160 to 228) were compared to
587 previously published N0 structures. The *N. meningitidis* PilQ N0 NMR structure
588 (purple, residues 350-417) is shown fit to the VcPilQ N0 (red) with the smallest
589 RMSD structure (0.9 Å) in (A) and with all structures (RMSD 0.9 to 1.2 Å) in
590 (B). (C) *S. typhimurium* InvG (PDB 6DV3, residues 34-104), RMSD 1.1 Å. (D)

591 The N0 domain of *Klebsiella oxytoca* PulD (PDB 6HCG, residues 27-100) RMSD
592 1.1 Å (Berry et al. 2012; Chernyatina and Low 2019; Worrall et al. 2016). Scale,
593 10 Å. **(E)** Table of RMSD results comparing VcPilQ N0 domain to other N0
594 domains.

595 **Supplemental Figure 11: Comparison of VcPilQ with putative *M. xanthus***
596 **PilQ structure**

597 **(A)** The domain organization of *V. cholerae* PilQ (top) and *M. xanthus* PilQ
598 (bottom) calculated in CDVist (Adebali, Ortega, and Zhulin 2015). **(B)** The
599 structure of VcPilQ (this study) in dark red is compared to the Phyre2 homology
600 modeling prediction of the MxPilQ structure (right, pink)(Kelley et al. 2015).

601 **Supplemental Movie 1: Atomic model of VcPilQ fit into the cryoEM density**

602 A single subunit of VcPilQ (labeled and colored by domain as in **Figure 1**) is
603 shown first by itself, then in the multimer. Next the model is displayed in the
604 cryoEM density to demonstrate agreement.

605

606 **Table 1.** Summary of single-particle data collection, 3D reconstruction, and model
607 refinement

Imaging parameters and 3D reconstruction	
Acceleration voltage (kV)	300
Magnification (X)	81,000
Pixel size (Å)	1.104
Frame rate (s ⁻¹)	0.092
Exposure time (s)	3.7
Total exposure (e ⁻ / Å)	60
Particles	
Micrographs used for selection	2,510
Defocus range (µm)	-0.5 to -3.5
Windowed	252,319
In final 3D reconstruction	100,543
Resolution	
'Gold-standard' at FSC 0.5 (Å)	3.0 Å
'Gold-standard' at FSC 0.143 (Å)	2.7 Å
Map-sharpening B factor (Å ²)	-69
Model refinement	
Resolution in phenix.real space refine (Å)	3.0
Model-to-map fit (CC_mask)	0.745
Number of atoms/residues/molecules	
NCS restrained chains	14
Protein atoms, residues (per chain)	43736, 412
Ramachandran angles (%)	
Favored	92.21
Allowed	7.79
Outliers	0
r.m.s. deviations	
Bond lengths (Å) Bond angles (°)	0.006
Bond angles (°)	0.847
Molprobit	
Score	2.81
Clashscore	10.53
Rotamer outliers (%)	10.91
EMRinger score	3.13

608

609

610 **Methods**

611 **Bacterial Strains and culture conditions**

612 All *V. cholerae* strains were derived from the El Tor strain E7946⁵⁴. Strains were
613 routinely grown in LB Miller broth and agar.

614 VcPilQ was purified from *V. cholerae* with a deca-histidine tag added to the N-
615 terminus of PilQ at the native locus. The full genotype of this strain (TND1751) is
616 10xHis-PilQ, Δ VC1807::SpecR, lacZ::lacIq, comEA-mCherry, Δ luxO, Ptac-tfoX,
617 Δ TCP::ZeoR, Δ MSHA::CarbR, Δ CTX::KanR.

618 For testing the impact of cysteine pair mutants on natural transformation, *V.*
619 *cholerae* strains were generated where the native copy of PilQ was deleted and the
620 corresponding PilQ allele was expressed at an ectopic site. The full genotype of the
621 parent strain (TND2140) was Δ lacZ::Pbad-10XHis-PilQ CmR, Δ pilQ::TetR,
622 Δ CTX::KanR, Δ MSHA::CarbR, Δ luxO, Δ TCP::ZeoR, comEA-mCherry, Ptac-
623 tfoX. The cysteine pair mutants were isogenic other than the cysteine mutations
624 introduced into the Pbad-10XHis-PilQ construct, which were PilQ S448C S453C
625 (TND2169) and PilQ L445C T493C (TND2170).

626 To test the impact of cysteine pair mutants on pilus biogenesis, *V. cholerae* strains
627 were generated akin to those described above, with the exception that the retraction
628 ATPase PilT was deleted and the strains contained a cysteine substitution mutation
629 in the major pilin that allows for competence pilus labeling as previously
630 described¹⁵. The full genotype of the parent strain (TND2244) was Δ lacZ::Pbad-
631 10XHis-PilQ CmR, Δ pilT::TmR, Δ pilQ::TetR, Δ CTX::KanR, Δ MSHA::CarbR,
632 Δ luxO, Δ TCP::ZeoR, pilA S67C, comEA-mCherry, Ptac-tfoX. The cysteine pair
633 mutants were isogenic other than the cysteine mutations introduced into the Pbad-
634 10XHis-PilQ construct, which were PilQ S448C S453C (TND2242) and PilQ
635 L445C T493C (TND2243).

636 All strains were generated by natural transformation and cotransformation exactly
637 as previously described ⁵⁵.

638 **Natural transformation assays**

639 Natural transformation assays were performed exactly as described in ¹⁵. For
640 reactions where strains harbored Pbad-10XHis-PilQ constructs, arabinose was
641 added to a final concentrations of 0.2%. Where indicated, DTT was added at the
642 indicated concentrations throughout the assay.

643 **Competence pilus labeling and microscopy**

644 Cells were labeled with AlexaFluor 488-maleimide dye and imaged to visualize
645 competence pili exactly as previously described ^{15,56}. All strains were grown with
646 arabinose added to a final concentrations of 0.2% to induce expression of the Pbad-
647 10XHis-PilQ construct. Where indicated, cells were grown in the presence of the
648 indicated concentration of DTT prior to labeling.

649 **Expression**

650 *Vibrio cholerae* expressing His-tagged PilQ (10xHis-PilQ, Δ VC1807::SpecR,
651 lacZ::lacIq, comEA-mCherry, Δ luxO, Ptac-tfoX, Δ TCP::ZeoR, Δ MSHA::CarbR,
652 Δ CTX::KanR) was streaked on Luria Broth agar plates and grown overnight at
653 30°C. Small cultures were seeded (5 mL) and grown over night at 30°C. The next
654 day, 500 mL cultures were seeded with the 5 mL culture. LB broth was
655 supplemented with 20 mM MgCl₂, 10 mM CaCl₂ and 100 μ M IPTG. The large
656 cultures were grown overnight at 30°C in beveled flasks. The following day,
657 cultures were spun down (6,000 rpm, 4°C, 20 minutes) and the cell paste was
658 weighed, aliquoted, and stored at -80°C.

659

660

661 **Purification**

662 Cell pellet (15 g) was resuspended in lysis buffer (50 mM Tris HCl, pH 8, 300 mM
663 NaCl, 1% DDM, 20 mM imidazole) supplemented with lysozyme (40 mg/mL in
664 50% glycerol/water), DNase I (4 mg/mL in 50% glycerol/water), and EDTA-free
665 Protease Inhibitor tablet (Roche, 11697498001). Lysis proceeded with stirring at
666 4°C for 20 hours. Lysate was clarified by ultracentrifugation (Beckman L8-M
667 ultracentrifuge, Rotor Type 45 Ti, 35,000rpm, 1 hour). The supernatant was mixed
668 with Ni NTA agarose beads (Anatrace, SUPER-NINTA25) and incubated with
669 stirring (4°C, 8 hours). In a gravity column at 4°C, proteins conjugated to Ni NTA
670 agarose beads were washed (50 mM Tris HCl, pH 8, 300 mM NaCl, 0.05% DDM,
671 70 mM imidazole), (50 mM Tris HCl, pH 8, 300 mM NaCl, 0.05% DDM, 300 mM
672 imidazole), and eluted (50 mM Tris HCl, pH 8, 300 mM NaCl, 0.05% DDM, 1 M
673 imidazole). Eluant was concentrated to ~1 mg/L (EMD Millipore Amicon Ultra-15,
674 30 kDa cutoff, UFC903024). Concentrated PilQ (150 µL of ~1 mg/mL protein) was
675 exchanged into Amphipol A8-35 (0.585 mg for a 3:1 ratio, Anatrace, A835) and
676 allowed to incubate at 4 C for 1 hr. Excess DDM was removed using Bio-Beads
677 SM2 (Bio-Rad, 1523920) by incubating overnight at 4°C. The protein was
678 concentrated.

679 **Electron microscopy**

680 For cryoEM, Quantifoil R2/2 300 Mesh grids (EMS, Q33100CR2) were glow
681 discharged (Pelco EasiGlow, 20 mA, 60 seconds). PilQ in amphipol (3 µL of ~0.8
682 mg/L) was frozen on a Mark IV Vitrobot (FEI, 20 °C, 100% relative humidity, blot
683 force -6, blot time 4 s). Micrographs were collected on a 300 kV Titan Krios
684 microscope (FEI) with energy filter (Gatan) and equipped with a K3 direct electron
685 detector (Gatan). Data was collected using Serial EM software with a pixel size of
686 1.104 Å (81,000x magnification) and a defocus range from -1.0 µm to -3.0 µm⁵⁷. A
687 fluence of 19.8 electrons/pixel/second was used with a 3.7 s exposure time to
688 collect 60 e-/Å².

689 **Image Processing**

690 The cryoEM image processing workflow is summarized in **Supplemental Figure**
691 **4**. MotionCor2 was used for motion correction and dose weighting of 3,808
692 movies⁵⁸. CTF correction was used to evaluate micrograph quality (Rohou and
693 Grigorieff 2015). CryoSPARC blob picking on 2,510 micrographs yielded
694 3,100,353 potential particles⁶⁰. After inspection, the 252,319 particles were
695 analyzed by several rounds of 2D classification and 3D classification to yield
696 100,543 particles. These particles were moved to Relion using the UCSF PyEM
697 package (<https://github.com/asarnow/pyem>) script⁶¹. In Relion, several rounds of
698 3D refinement, polishing and CTF refinement were used⁶²⁻⁶⁴. ResMap was used to
699 calculate local resolution³⁵.

700 **Model Building and Refinement**

701 The initial model (residues 230-571) was auto-built using Buccaneer⁶⁵. Subsequent
702 building and model adjustments were performed by hand using COOT⁶⁶. A
703 homology model of the N0 domain (residues 160-229) was created using I-
704 TASSER and manually docked using COOT^{42,67,68}. Coulombic potential density for
705 residues 1-159 were not observed. The model was refined in PHENIX version 1.16-
706 dev3549 using phenix.real_space_refine with the resolution set to 3 Å⁶⁹. NCS
707 constraints were applied for the 14 subunits and were automatically detected and
708 refined. Automatically determined secondary structure restraints, rotamer restraints,
709 and Ramachandran restraints were applied as well. The quality of the model was
710 evaluated using EMRinger⁷⁰ and Molprobit⁷¹ (Table 1).

711 **Mass Spectrometry**

712 After running a BioRad Stain Free gel and performing a coomassie staining, the
713 band of interest was excised with a clean razor blade. The gel piece was destained
714 with ammonium bicarbonate and reduced with DTT (50°C, 30 minutes). Next the
715 sample was alkylated with iodoacetamide (room temperature, dark, 20 minutes).

716 The gel pieces were then dehydrated. Trypsin was used to digest the protein in the
717 gel (37°C, overnight). Peptides were extracted from the gel matrix, dried, and de
718 salted with a zip tip.

719 The in-gel-digested samples were subjected to LC-MS/MS analysis on a nanoflow
720 LC system, EASY-nLC 1200, (Thermo Fisher Scientific) coupled to a QExactive
721 HF Orbitrap mass spectrometer (Thermo Fisher Scientific, Bremen, Germany)
722 equipped with a Nanospray Flex ion source.

723 Samples were directly loaded onto a C18 Aurora series column (Ion Opticks,
724 Parkville, Australia). The 25cm x 50µm ID column (1.6 µm) was heated to 45° C.
725 The peptides were separated with a 60 min gradient at a flow rate of 350 nL/min.
726 The gradient was as follows: 2–6% Solvent B (3.5 min), 6-25% B (42.5 min), and
727 25-40% B (14.5min), to 100% B (1min) and 100% B (12min). Solvent A consisted
728 of 97.8% H₂O, 2% ACN, and 0.2% formic acid and solvent B consisted of 19.8%
729 H₂O, 80% ACN, and 0.2% formic acid.

730 The QExactive HF Orbitrap was operated in data dependent mode. Spray voltage
731 was set to 1.8 kV, S-lens RF level at 50, and heated capillary at 275 °C. Full scan
732 resolution was set to 60,000 at m/z 200. Full scan target was 3×10^6 with a
733 maximum injection time of 15 ms (profile mode). Mass range was set to 300–1650
734 m/z. For data dependent MS₂ scans the loop count was 12, target value was set at 1
735 $\times 10^5$, and intensity threshold was kept at 1×10^5 . Isolation width was set at 1.2 m/z
736 and a fixed first mass of 100 was used. Normalized collision energy was set at 28.
737 Peptide match was set to off, and isotope exclusion was on. Ms₂ data was collected
738 in centroid mode.

739 Raw data were analyzed using MaxQuant (v. 1.6.5.0)^{72,73}. Spectra were searched
740 against UniProt *V. cholerae* entries (3784 sequences) and a contaminant protein
741 database (246 sequences). Trypsin was specified as the digestion enzyme and up to
742 two missed cleavages were allowed. Precursor mass tolerance was 4.5 ppm after
743 recalibration and fragment mass tolerance was 20 ppm. Variable modifications

744 included oxidation of methionine and protein N-terminal acetylation.
745 Carbamidomethylation of cysteine was specified as a fixed modification. A decoy
746 database was used to set score thresholds to ensure a 1% false discovery rate at the
747 protein and peptide level. Protein abundances were estimated using iBAQ and the
748 fractional abundance was calculated as the protein abundance divided by the sum of
749 all non-contaminant protein abundances⁷⁴.

750 **Author Contributions**

751 S.J.W. conceptualized the project, expressed and purified the protein, prepared
752 samples for cryoEM, collected cryoEM data, processed cryoEM data, assisted
753 in atomic model building, interpreted results, designed figures, and wrote the
754 paper.

755 M.S. purified protein, assisted with cryoEM sample prep and data collection,
756 built the atomic model, interpreted results, and provided feedback on the
757 paper.

758 T.D. engineered the *V. cholerae* constructs, performed microbial assays, and
759 interpreted results.

760 A.D. conceptualized the project, obtained funding, engineered the *V. cholerae*
761 constructs, performed microbial assays, interpreted results, designed figures,
762 and provided feedback on the paper.

763 G.J.J. conceptualized the project, obtained funding, and provided feedback on
764 the paper.

765 **Competing interests statement**

766 The authors declare no competing interests.

767 **Acknowledgements**

768 Cryo Electron microscopy was performed in the Beckman Institute Resource
769 Center for Transmission Electron Microscopy at Caltech. Dr. Songye Chen and Dr.
770 Andrey Malyutin assisted with data collection. Dr. Spiros D. Garbis, Dr. Annie
771 Moradian, Dr. Michael Sweredoski, and Dr. Brett Lomenick at the Caltech
772 Proteome Exploration Laboratory (PEL) performed and analyzed mass
773 spectrometry results. Dr. Naima Sharaf, Jeffery Lai, and Prof. Doug Rees provided
774 invaluable advice on membrane protein biochemistry and instrumentation. Jane
775 Ding and Welison Floriano provided computational support. Dr. Debnath Ghosal,
776 Dr. Mohammed Kaplan, Dr. Davi Ortega, Dr. Catherine Oikonomou, Dr. Lauren
777 Ann Metskas, Dr. Christopher Barnes, Claudia Jette, and Andrew Schacht provided
778 feedback and advice. This work was supported in part by grant R35GM128674
779 from the National Institutes of Health to A.B.D.

References

1. von Wintersdorff, C. J. H. *et al.* Dissemination of Antimicrobial Resistance in Microbial Ecosystems through Horizontal Gene Transfer. *Front. Microbiol.* **7**, (2016).
2. Blokesch, M. In and out—contribution of natural transformation to the shuffling of large genomic regions. *Current Opinion in Microbiology* **38**, 22–29 (2017).
3. Goodgal, S. H. DNA uptake in Haemophilus transformation. *Annu. Rev. Genet.* **16**, 169–192 (1982).
4. Mell, J. C., Shumilina, S., Hall, I. M. & Redfield, R. J. Transformation of natural genetic variation into Haemophilus influenzae genomes. *PLoS Pathog.* **7**, e1002151 (2011).
5. Mell, J. C. & Redfield, R. J. Natural Competence and the Evolution of DNA Uptake Specificity. *Journal of Bacteriology* **196**, 1471–1483 (2014).
6. Maiden, M. C. J. Horizontal Genetic Exchange, Evolution, and Spread of Antibiotic Resistance in Bacteria. *Clinical Infectious Diseases* **27**, S12–S20 (1998).
7. Domingues, S. *et al.* Natural Transformation Facilitates Transfer of Transposons, Integrons and Gene Cassettes between Bacterial Species. *PLoS Pathog* **8**, (2012).
8. Blokesch, M. & Schoolnik, G. K. Serogroup conversion of Vibrio cholerae in aquatic reservoirs. *PLoS pathogens* **3**, (2007).
9. Miller, M. C., Keymer, D. P., Avelar, A., Boehm, A. B. & Schoolnik, G. K. Detection and transformation of genome segments that differ within a coastal population of Vibrio cholerae strains. *Appl. Environ. Microbiol.* **73**, 3695–3704 (2007).
10. Croucher, N. J. *et al.* Rapid Pneumococcal Evolution in Response to Clinical Interventions. *Science* **331**, 430–434 (2011).

11. Hu, D. *et al.* Origins of the current seventh cholera pandemic. *PNAS* **113**, E7730–E7739 (2016).
12. Meibom, K. L., Blokesch, M., Dolganov, N. A., Wu, C.-Y. & Schoolnik, G. K. Chitin Induces Natural Competence in *Vibrio cholerae*. *Science* **310**, 1824–1827 (2005).
13. Meibom, K. L. *et al.* The *Vibrio cholerae* chitin utilization program. *Proceedings of the National Academy of Sciences of the United States of America* **101**, 2524–2529 (2004).
14. Piepenbrink, K. H. DNA Uptake by Type IV Filaments. *Frontiers in Molecular Biosciences* **6**, 1 (2019).
15. Ellison, C. K. *et al.* Retraction of DNA-bound type IV competence pili initiates DNA uptake during natural transformation in *Vibrio cholerae*. *Nature Microbiology* **3**, 773–780 (2018).
16. Sandkvist, M. Biology of type II secretion. *Molecular Microbiology* **40**, 271–283 (2001).
17. Korotkov, K. V., Gonen, T. & Hol, W. G. Secretins: dynamic channels for protein transport across membranes. *Trends in biochemical sciences* **36**, (2011).
18. Majewski, D. D., Worrall, L. J. & Strynadka, N. C. Secretins revealed: structural insights into the giant gated outer membrane portals of bacteria. *Current Opinion in Structural Biology* **51**, 61–72 (2018).
19. Genin, S. & Boucher, C. A. A superfamily of proteins involved in different secretion pathways in gram-negative bacteria: modular structure and specificity of the N-terminal domain. *Molec. Gen. Genet.* **243**, 112–118 (1994).
20. Berry, J.-L. *et al.* Structure and Assembly of a Trans-Periplasmic Channel for Type IV Pili in *Neisseria meningitidis*. *Plos Pathog* **8**, e1002923 (2012).

21. Burkhardt, J., Vonck, J., Langer, J. D., Salzer, R. & Averhoff, B. Unusual N-terminal $\alpha\beta\alpha\beta\beta\alpha$ fold of PilQ from *Thermus thermophilus* mediates ring formation and is essential for piliation. **287**, 8484–94 (2012).
22. de Souza, R. F., Anantharaman, V., de Souza, S. J., Aravind, L. & Gueiros-Filho, F. J. AMIN domains have a predicted role in localization of diverse periplasmic protein complexes. *Bioinformatics* **24**, 2423–2426 (2008).
23. Green, E. R. & Mecsas, J. Bacterial Secretion Systems – An overview. *Microbiology spectrum* **4**, 215–239 (2016).
24. Yan, Z., Yin, M., Xu, D., Zhu, Y. & Li, X. Structural insights into the secretin translocation channel in the type II secretion system. **24**, 177–183 (2017).
25. Hay, I. D., Belousoff, M. J., Dunstan, R. A., Bamert, R. S. & Lithgow, T. Structure and Membrane Topography of the Vibrio-Type Secretin Complex from the Type 2 Secretion System of Enteropathogenic *Escherichia coli*. *Journal of bacteriology* **200**, (2018).
26. Yin, M., Yan, Z. & Li, X. Structural insight into the assembly of the type II secretion system pilotin–secretin complex from enterotoxigenic *Escherichia coli*. *Nature Microbiology* **3**, 581–587 (2018).
27. Hay, I. D., Belousoff, M. J. & Lithgow, T. Structural Basis of Type 2 Secretion System Engagement between the Inner and Outer Bacterial Membranes. *mBio* **8**, e01344–17 (2017).
28. Chernyatina, A. A. & Low, H. H. Architecture of a bacterial type II secretion system. *bioRxiv* 397794 (2018) doi:10.1101/397794.

29. Howard, P. S. *et al.* Structure and assembly of pilotin-dependent and -independent secretins of the type II secretion system. *PLOS Pathogens* **15**, e1007731 (2019).
30. Worrall, L. *et al.* Near-atomic-resolution cryo-EM analysis of the Salmonella T3S injectisome basal body. *Nature* **540**, 597 (2016).
31. Chami, M. *et al.* Structural Insights into the Secretin PulD and Its Trypsin-resistant Core. *Journal of Biological Chemistry* **280**, 37732–37741 (2005).
32. Guilvout, I., Nickerson, N. N., Chami, M. & Pugsley, A. P. Multimerization-defective variants of dodecameric secretin PulD. *Research in Microbiology* **162**, 180–190 (2011).
33. Cheng, A. *et al.* High resolution single particle cryo-electron microscopy using beam-image shift. *J. Struct. Biol.* **204**, 270–275 (2018).
34. Tan, Y. *et al.* Addressing preferred specimen orientation in single-particle cryo-EM through tilting. *Nature Methods* **14**, 793–796 (2017).
35. Kucukelbir, A., Sigworth, F. J. & Tagare, H. D. Quantifying the local resolution of cryo-EM density maps. *Nature Methods* **11**, 63–65 (2014).
36. Balasingham, S. V. *et al.* Interactions between the Lipoprotein PilP and the Secretin PilQ in *Neisseria meningitidis* ∇ \dagger . *Journal of Bacteriology* **189**, 5716–5727 (2007).
37. Pettersen, E. F. *et al.* UCSF Chimera—A visualization system for exploratory research and analysis. *Journal of Computational Chemistry* **25**, 1605–1612 (2004).
38. Chernyatina, A. A. & Low, H. H. Core architecture of a bacterial type II secretion system. *bioRxiv* 397794 (2019) doi:10.1101/397794.
39. Craig, D. B. & Dombkowski, A. A. Disulfide by Design 2.0: a web-based tool for disulfide engineering in proteins. *BMC Bioinformatics* **14**, 346 (2013).

40. Dombkowski, A. A. Disulfide by Design: a computational method for the rational design of disulfide bonds in proteins. *Bioinformatics* **19**, 1852–1853 (2003).
41. Dombkowski, A. A., Sultana, K. Z. & Craig, D. B. Protein disulfide engineering. *FEBS Lett.* **588**, 206–212 (2014).
42. Zhang, Y. I-TASSER server for protein 3D structure prediction. *BMC Bioinformatics* **9**, 40 (2008).
43. Lomize, M. A., Pogozheva, I. D., Joo, H., Mosberg, H. I. & Lomize, A. L. OPM database and PPM web server: resources for positioning of proteins in membranes. *Nucleic Acids Res.* **40**, D370-376 (2012).
44. Chang, Y.-W. *et al.* Architecture of the type IVa pilus machine. *Science* **351**, aad2001 (2016).
45. Adebali, O., Ortega, D. R. & Zhulin, I. B. CDvist: a webserver for identification and visualization of conserved domains in protein sequences. *Bioinformatics* **31**, 1475–1477 (2015).
46. Kelley, L. A., Mezulis, S., Yates, C. M., Wass, M. N. & Sternberg, M. J. E. The Phyre2 web portal for protein modeling, prediction and analysis. *Nature Protocols* **10**, 845–858 (2015).
47. Siewering, K. *et al.* Peptidoglycan-binding protein TsaP functions in surface assembly of type IV pili. *Proceedings of the National Academy of Sciences* **111**, E953–E961 (2014).
48. Phillips, R. Membranes by the Numbers. *arXiv:1703.02066 [cond-mat, physics:physics, q-bio]* (2017).

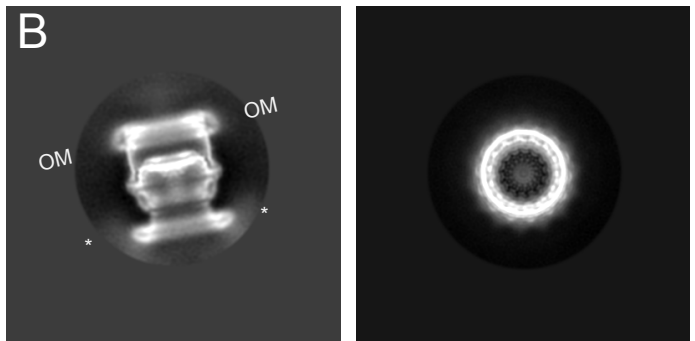
49. Craig, L., Pique, M. E. & Tainer, J. A. Type IV pilus structure and bacterial pathogenicity. *Nature Reviews Microbiology* **2**, 363 (2004).
50. Kolappan, S. *et al.* Structure of the *Neisseria meningitidis* Type IV pilus. *Nature Communications* **7**, 13015 (2016).
51. Wang, F. *et al.* Cryoelectron Microscopy Reconstructions of the *Pseudomonas aeruginosa* and *Neisseria gonorrhoeae* Type IV Pili at Sub-nanometer Resolution. *Structure* **25**, 1423–1435.e4 (2017).
52. Bardiaux, B. *et al.* Structure and Assembly of the Enterohemorrhagic *Escherichia coli* Type 4 Pilus. *Structure (London, England: 1993)* (2019) doi:10.1016/j.str.2019.03.021.
53. Neuhaus, A. *et al.* A new twist on bacterial motility – two distinct type IV pili revealed by cryoEM. *bioRxiv* 720938 (2019) doi:10.1101/720938.
54. Miller, V. L., DiRita, V. J. & Mekalanos, J. J. Identification of *toxS*, a regulatory gene whose product enhances *toxR*-mediated activation of the cholera toxin promoter. *J. Bacteriol.* **171**, 1288–1293 (1989).
55. Dalia, A. B. Natural Cotransformation and Multiplex Genome Editing by Natural Transformation (MuGENT) of *Vibrio cholerae*. in *Vibrio Cholerae: Methods and Protocols* (ed. Sikora, A. E.) 53–64 (Springer, 2018). doi:10.1007/978-1-4939-8685-9_6.
56. Ellison, C. K., Dalia, T. N., Dalia, A. B. & Brun, Y. V. Real-time microscopy and physical perturbation of bacterial pili using maleimide-conjugated molecules. *Nat Protoc* **14**, 1803–1819 (2019).

57. Mastronarde, D. N. Automated electron microscope tomography using robust prediction of specimen movements. *Journal of Structural Biology* **152**, 36–51 (2005).
58. Zheng, S. Q. *et al.* MotionCor2: anisotropic correction of beam-induced motion for improved cryo-electron microscopy. *Nature Methods* (2017) doi:10.1038/nmeth.4193.
59. Rohou, A. & Grigorieff, N. CTFFIND4: Fast and accurate defocus estimation from electron micrographs. **192**, 216–221 (2015).
60. Punjani, A., Rubinstein, J. L., Fleet, D. J. & Brubaker, M. A. cryoSPARC: algorithms for rapid unsupervised cryo-EM structure determination. *Nature Methods* **14**, (2017).
61. Daniel Asarnow, Eugene Palovcak & Yifan Cheng. *asarnow/pyem: UCSF pyem v0.5*. (Zenodo, 2019). doi:10.5281/zenodo.3576630.
62. Kimanius, D., Forsberg, B. O., Scheres, S. & Lindahl, E. Accelerated cryo-EM structure determination with parallelisation using GPUs in RELION-2. 059717 (2016) doi:10.1101/059717.
63. Zivanov, J. *et al.* New tools for automated high-resolution cryo-EM structure determination in RELION-3. *eLife* **7**, e42166 (2018).
64. Zivanov, J., Nakane, T. & Scheres, S. H. W. Estimation of High-Order Aberrations and Anisotropic Magnification from Cryo-EM Datasets in RELION-3.1. *bioRxiv* 798066 (2019) doi:10.1101/798066.
65. Cowtan, K. The Buccaneer software for automated model building. 1. Tracing protein chains. *Acta Crystallographica Section D: Biological Crystallography* **62**, 1002–11 (2006).
66. Emsley, P., Lohkamp, B., Scott, W. G. & Cowtan, K. Features and development of Coot. *Acta Cryst D* **66**, 486–501 (2010).

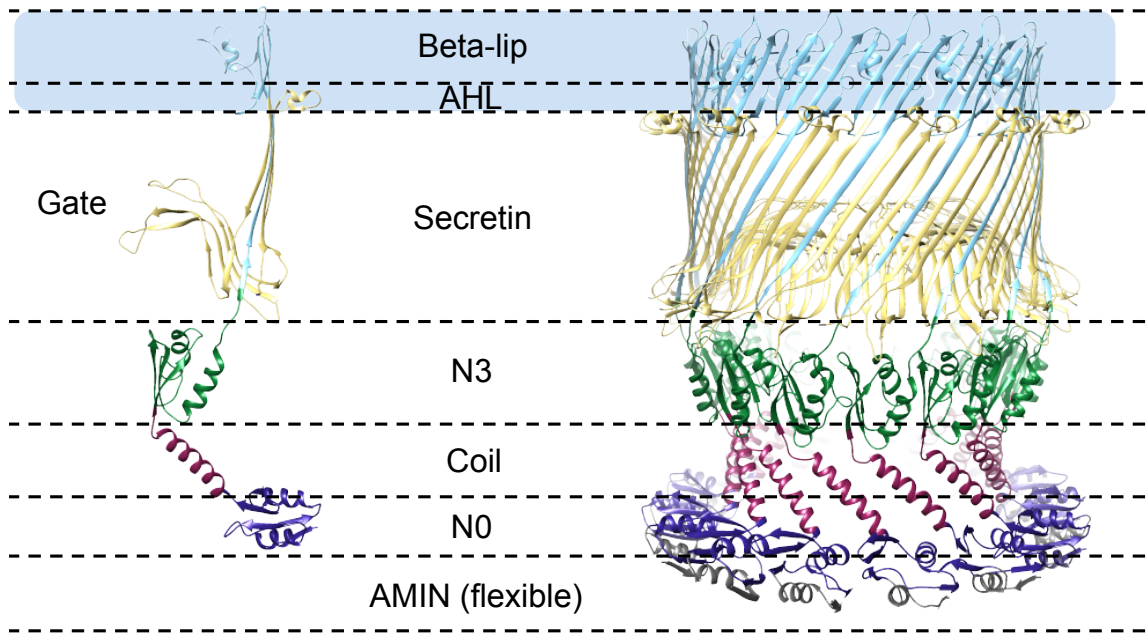
67. Roy, A., Kucukural, A. & Zhang, Y. I-TASSER: a unified platform for automated protein structure and function prediction. *Nat Protoc* **5**, 725–738 (2010).
68. Yang, J. *et al.* The I-TASSER Suite: protein structure and function prediction. *Nature Methods* **12**, 7–8 (2015).
69. Adams, P. D. *et al.* PHENIX: a comprehensive Python-based system for macromolecular structure solution. *Acta Cryst D* **66**, 213–221 (2010).
70. Barad, B. A. *et al.* EMRinger: side chain-directed model and map validation for 3D cryo-electron microscopy. (2015) doi:10.1038/nmeth.3541.
71. Chen, V. B. *et al.* MolProbity: all-atom structure validation for macromolecular crystallography. *Acta Cryst D* **66**, 12–21 (2010).
72. Cox, J. *et al.* Andromeda: A Peptide Search Engine Integrated into the MaxQuant Environment. *J. Proteome Res.* **10**, 1794–1805 (2011).
73. Cox, J. & Mann, M. MaxQuant enables high peptide identification rates, individualized p.p.b.-range mass accuracies and proteome-wide protein quantification. *Nat Biotechnol* **26**, 1367–1372 (2008).
74. Schwanhäusser, B. *et al.* Global quantification of mammalian gene expression control. *Nature* **473**, 337–342 (2011).

Figure 1

A



C



D

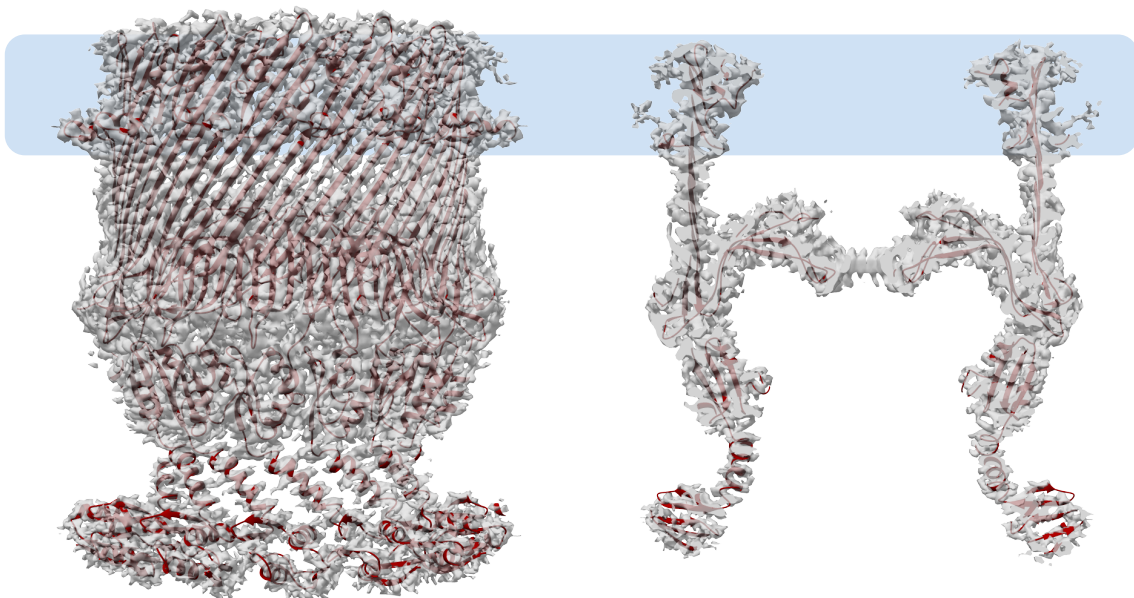
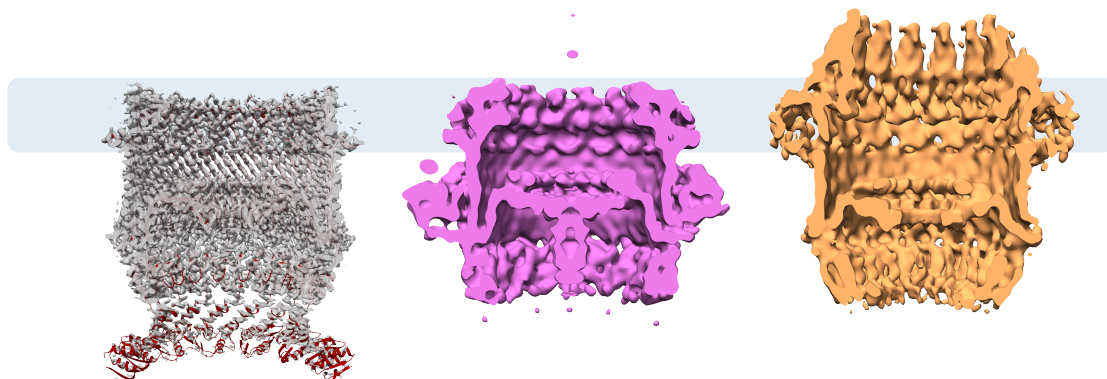


Figure 2

A



B

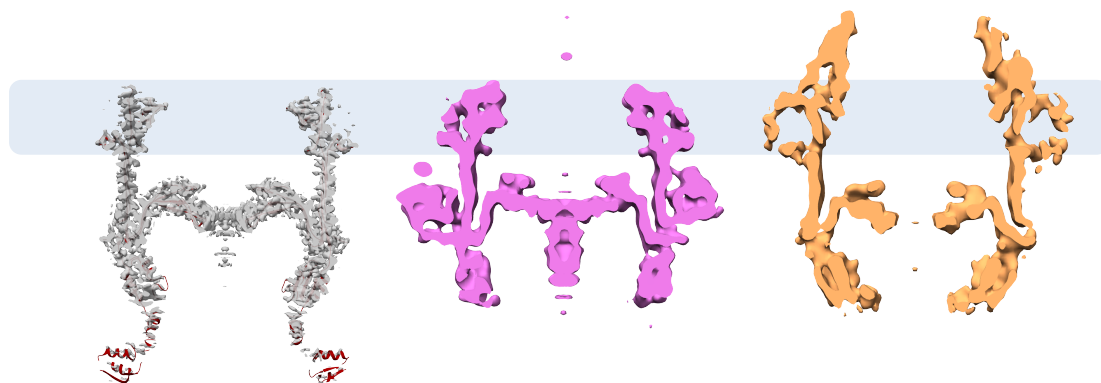


Figure 3

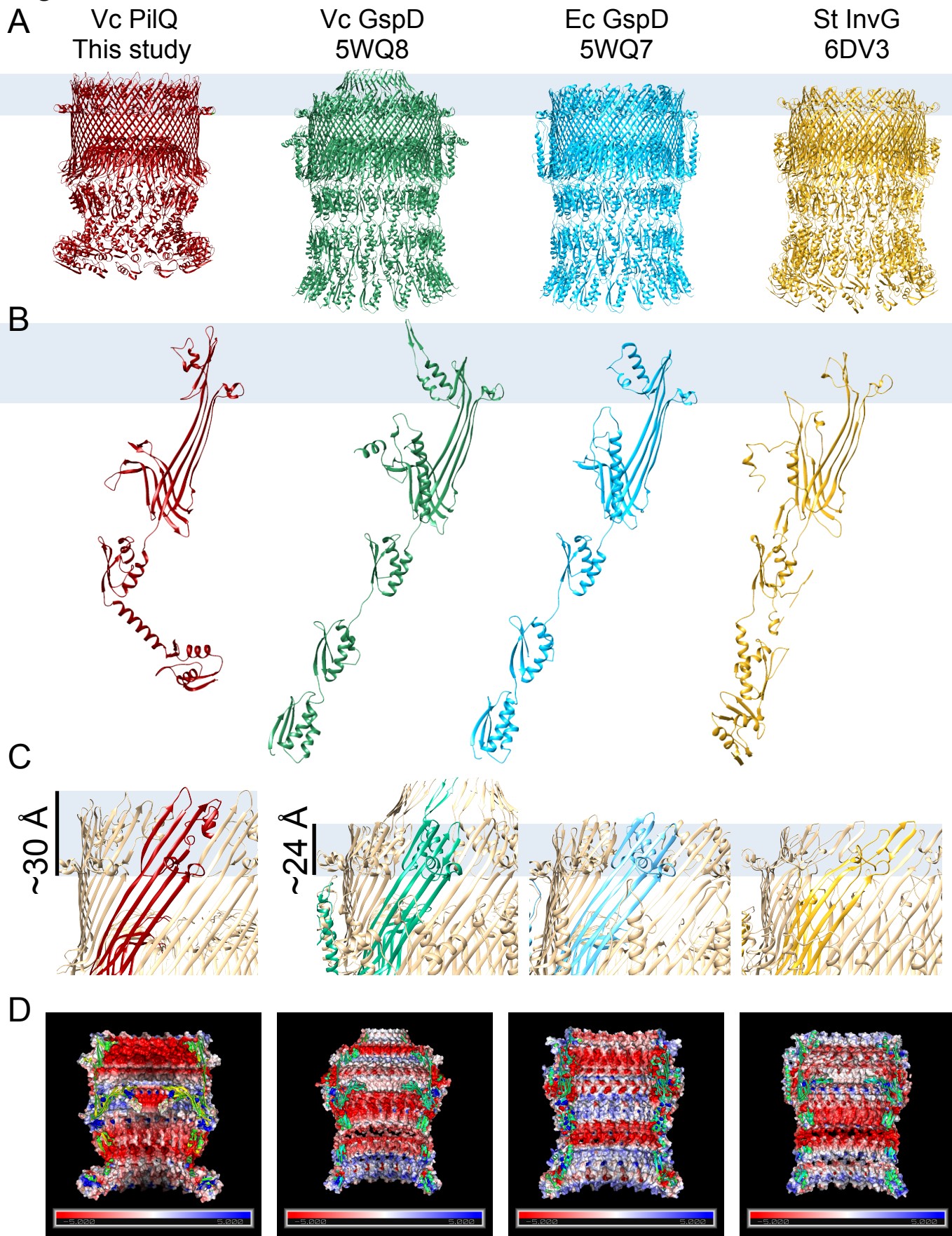
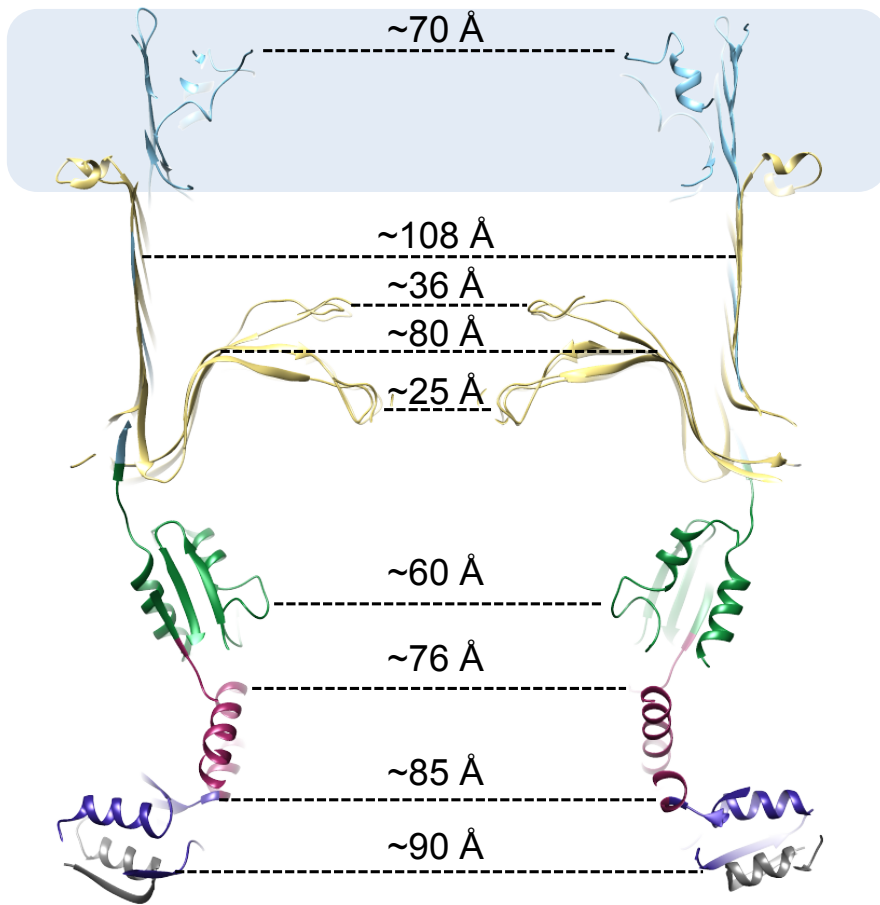


Figure 4

A



B

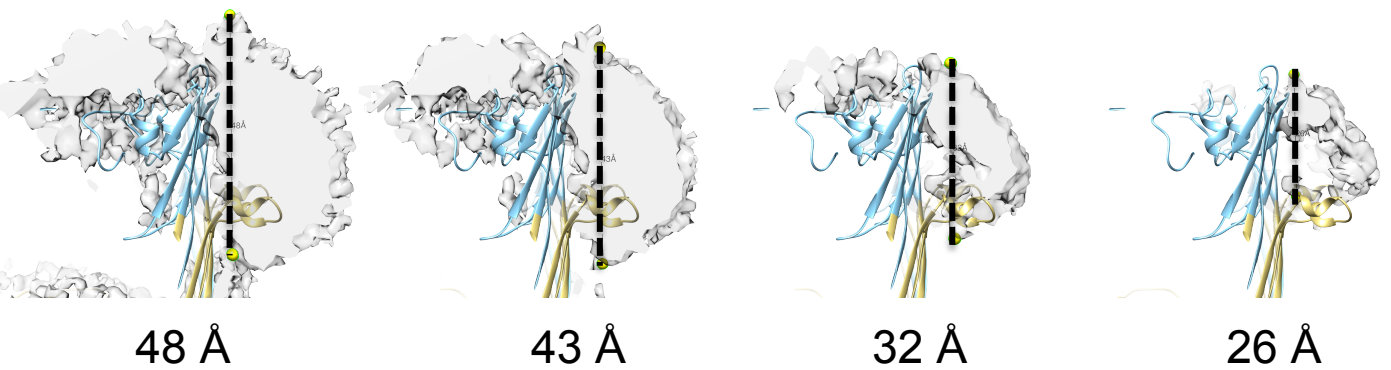
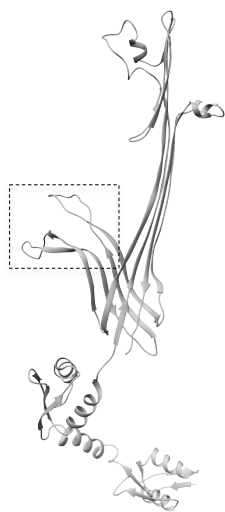
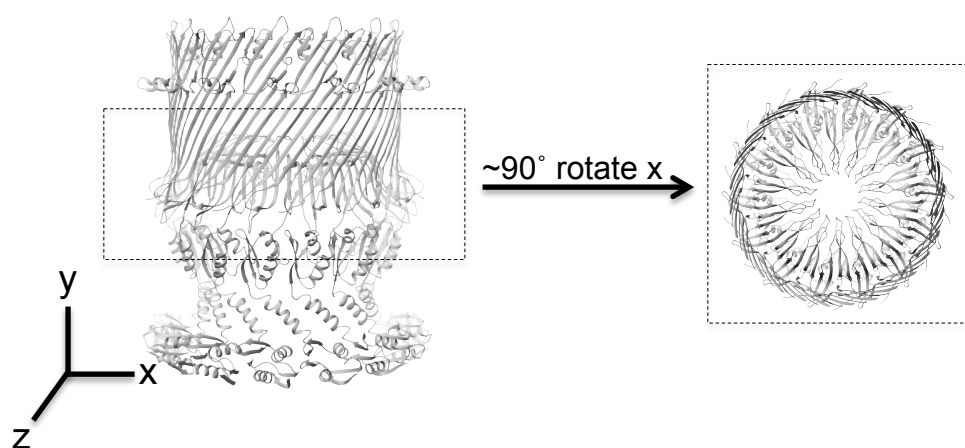


Figure 5

A

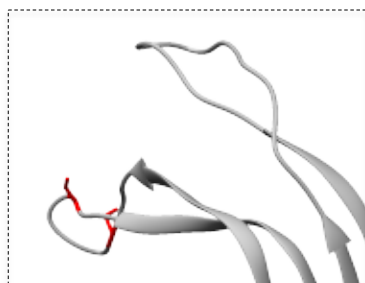


B



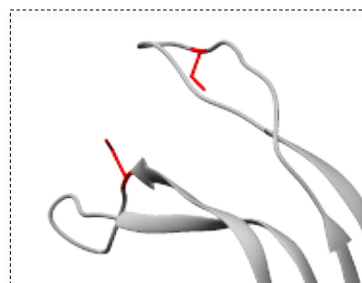
C

S448C/S453C



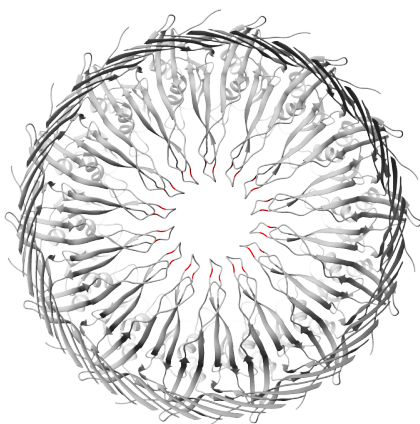
D

L445C/T493C



E

S448C/S453C



F

L445C/T493C

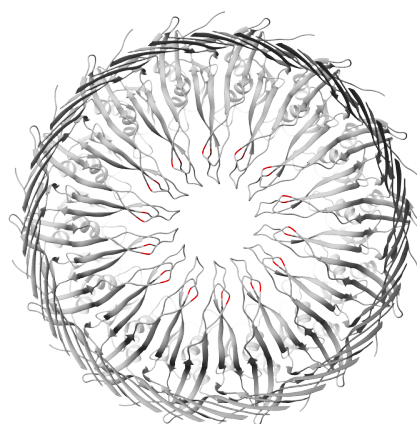
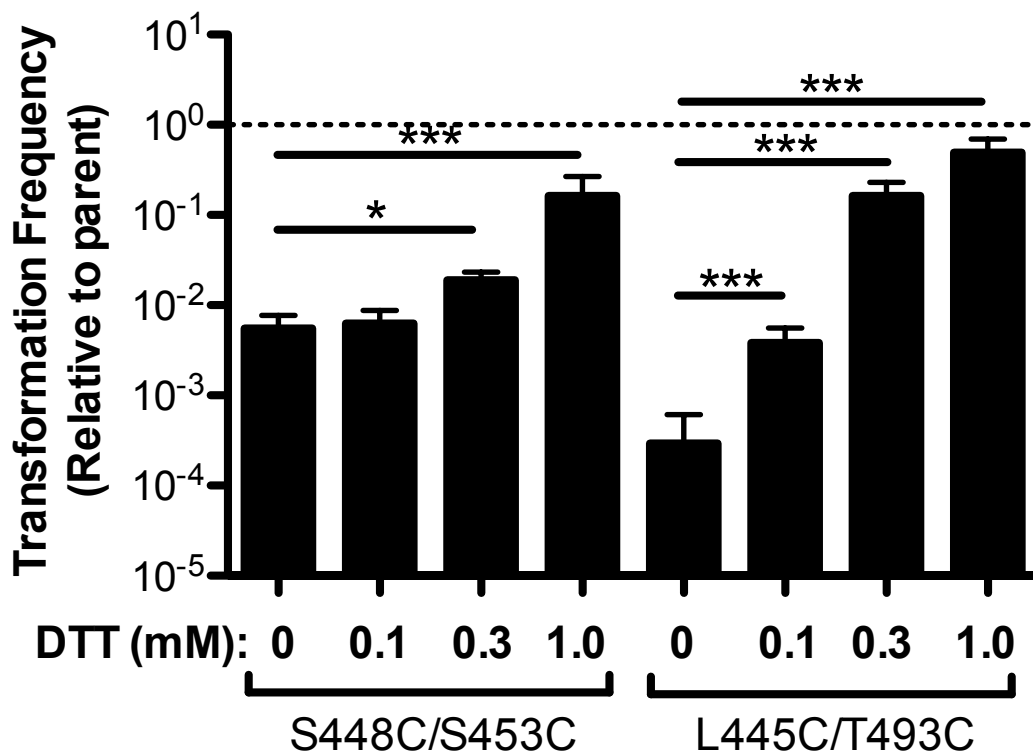


Figure 6

A



B

C

D

0mM DTT

1mM DTT

2mM DTT

S448C
S453C

L445C
T493C

WT

S448C
S453C

L445C
T493C

WT

S448C
S453C

L445C
T493C

WT

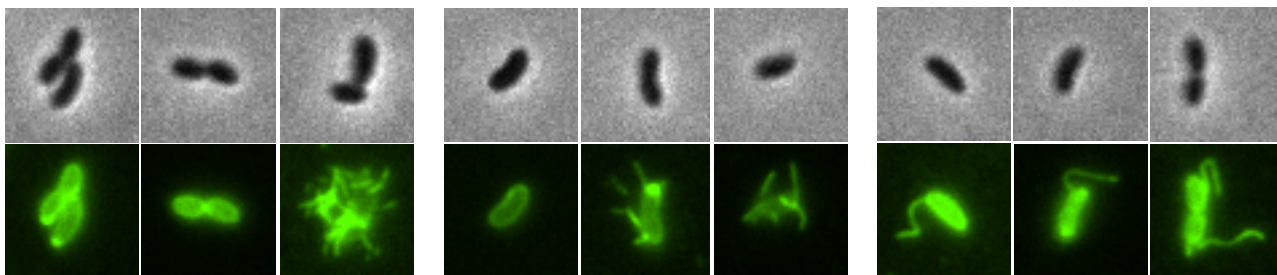


Figure 7

